Three-Dimensional Gas Exchange Pathways in Pome Fruit Characterized by Synchrotron X-Ray Computed Tomography[1][C][W][OA]

Pieter Verboven*, Greet Kerckhofs, Hibru Kelemu Mebatsion, Quang Tri Ho, Kristiaan Temst, Martine Wevers, Peter Cloetens, and Bart M. Nicolaï

Division BIOSYST-MeBioS (P.V., H.K.M., B.M.N.), Research Group of Materials Performance and Non-Destructive Evaluation (G.K., M.W.), and Nuclear and Radiation Physics Section (K.T.), Katholieke Universiteit Leuven, BE–3001 Leuven, Belgium; and European Synchrotron Radiation Facility, 38043 Grenoble cedex, France (P.C.)

Our understanding of the gas exchange mechanisms in plant organs critically depends on insights in the three-dimensional (3-D) structural arrangement of cells and voids. Using synchrotron radiation x-ray tomography, we obtained for the first time high-contrast 3-D absorption images of in vivo fruit tissues of high moisture content at 1.4-μm resolution and 3-D phase contrast images of cell assemblies at a resolution as low as 0.7 μm, enabling visualization of individual cell morphology, cell walls, and entire void networks that were previously unknown. Intercellular spaces were always clear of water. The apple (*Malus domestica*) cortex contains considerably larger parenchyma cells and voids than pear (*Pyrus communis*) parenchyma. Voids in apple often are larger than the surrounding cells and some cells are not connected to void spaces. The main voids in apple stretch hundreds of micrometers but are disconnected. Voids in pear cortex tissue are always smaller than parenchyma cells, but each cell is surrounded by a tight and continuous network of voids, except near brachysscleroid groups. Vascular and dermal tissues were also measured. The visualized network architecture was consistent over different picking dates and shelf life. The differences in void fraction (5.1% for pear cortex and 23.0% for apple cortex) and in gas network architecture helps explain the ability of tissues to facilitate or impede gas exchange. Structural changes and anisotropy of tissues may eventually lead to physiological disorders. A combined tomography and internal gas analysis during growth are needed to make progress on the understanding of void formation in fruit.

Gas exchange of plants with their environment is essential for metabolic processes such as photosynthesis and respiration. In roots and bulky storage organs such as fruit and tubers, insufficient exchange of O_2 and CO_2 might lead to anoxia, physiological changes, and eventually cell death (Denison, 1992; Drew, 1997; Geigenberger et al., 2000; Franck et al., 2007). Because gas exchange to a large extent depends on the structural arrangement of cells and intercellular spaces (Parkhurst and Mott, 1990; Aalto and Juurola, 2002; Cloetens et al., 2006; Mendoza et al., 2007), visualization and quantification of the tissue microstructure improves our understanding of exchange mechanisms.

The complex three-dimensional (3-D) organization of cells in tissues is today recognized as an important aspect of cell biology research (Abbott, 2003). The interest in 3-D imaging techniques at micrometer and submicrometer scales to visualize biological microstructures has consequently grown, today even at nanometer scales in individual cells (Larabell and Le Gros, 2003; Attwood, 2006). In tissues, the structural arrangements of cells create specific pathways for transport of chemical compounds to and from cells. Visualization of these pathways by x-ray microtomography of tissues in their natural state has been difficult, because of the low contrast and limited resolution (Westneat et al., 2003; Kuroki et al., 2004; Kim et al., 2006; Rau et al., 2006; Mendoza et al., 2007). Important features such as small voids between cells, vascular capillaries, or cell walls could therefore not be visualized, rendering incorrect connectivity information. Further, individual cells have not yet been distinguished in images obtained by absorption mode x-ray tomography.

Phase contrast imaging has been developed for edge enhancement on tomographs with low absorption mode contrast (Davis et al., 1995; Cloetens et al., 1999). High-resolution phase tomography of biological

[1] This work was supported by the European Synchrotron Radiation Facility (beamtime experiment no. MA222) and Katholieke Universiteit Leuven (project nos. IDO/00/008 and OT 04/31; PhD scholarships to H.K.M. and Q.T.H.). This research was carried out in the framework of European Union COST action 924.

* Corresponding author; e-mail pieter.verboven@biw.kuleuven.be.

The author responsible for distribution of materials integral to the findings presented in this article in accordance with the policy described in the Instructions for Authors (www.plantphysiol.org) is: Pieter Verboven (pieter.verboven@biw.kuleuven.be).

[C] Some figures in this article are displayed in color online but in black and white in the print edition.

[W] The online version of this article contains Web-only data.

[OA] Open Access articles can be viewed online without a subscription.

www.plantphysiol.org/cgi/doi/10.1104/pp.108.118935

tissues at a pixel size close to 1 μm has only recently been achieved (Plouraboue et al., 2004; Thurner et al., 2005), but required sample preparation to improve contrast on the images. For in vivo observations, high-resolution phase tomography has so far only been applied to relatively dry- or hard-biological samples, such as plant seeds (Stuppy et al., 2003; Cloetens et al., 2006). Wet, soft samples are more susceptible to damage by the x-rays. Diffraction imaging has been achieved on individual cells at resolutions better than x-ray optical devices (Miao et al., 2003; Shapiro et al., 2005), but larger samples that represent entire tissues require other techniques (Cloetens et al., 2006).

High resolution phase tomography using synchrotron radiation is used here to explore at submicrometer resolution 3-D plant tissues with high water content in their natural state. As explained by Salvo et al. (2003), synchrotron radiation x-ray tomography has important advantages over x-ray tube tomography. X-ray tube tomography produces a divergent beam; therefore the resolution is limited by the beam angle and the required field of view. The beam angle may also produce artefacts in the reconstructed images. The parallel beam produced by synchrotron radiation with good spatial coherence makes a quantitative reconstruction, free of geometrical and beam hardening artefacts, possible. These conditions can only be achieved at large-scale facilities that produce high-energy flux sources and long distances between source and tomography setup (on the order of 100 m). The facility at the European Synchrotron Radiation Facility (Grenoble, France) was accessible to the authors on the basis of a successful research proposal.

In plants, tissue structure determines to a large extent the internal pathways for gas exchange (Colmer, 2003). Insufficient exchange of O_2 and CO_2 leads to altered cellular metabolism and can dramatically change plant growth (Drew, 1997; Fukao and Bailey-Serres, 2004). The effect of the actual 3-D tissue structure of plant organs has long been put forward but not yet quantified for explaining gas exchange in plant tissues (Parkhurst and Mott, 1990; Lawson and Morison, 2006). In this research we have considered fruits of apple (*Malus* $\times$ *domestica* 'Jonagold') and pear (*Pyrus communis* 'Conference') because their gas exchange properties have been shown to be very different (Schotsmans et al., 2004; Ho et al., 2006). The storage life of these fruits and, hence, their year-round availability to consumers critically depends on their gas exchange properties (Ho et al., 2006). In some fruits such as pears, which are typically stored under a controlled atmosphere with reduced O_2 and increased CO_2 levels to extend their commercial storage life, anoxia and consequent physical disorders such as browning may occur, eventually leading to cell death and loss of the product (Franck et al., 2007). Similar atmosphere conditions, however, do not seem to affect other fruit such as apples appreciably (Saquet et al., 2000). Although it is likely that this is related to differences in concentration gradients resulting from differences in tissue diffusivity and respiratory activity, there is little information about such gas gradients in fruit in the literature. Such knowledge would be, nevertheless, very valuable both to understand gas exchange in plant tissue but also to guide commercial storage practices because disorders under controlled atmosphere related to fermentation are a prime cause of concern.

Fresh samples from skin tissue, cortex tissue, and vascular tissue of the fruits were imaged. To directly observe voids in the different tissues of the fruit, we obtained high-resolution and high-contrast absorption mode x-ray images of fresh fruit samples using synchrotron x-rays at 1.4 and 5.1 μm pixel resolution. Next, phase contrast x-ray tomography allowed for edge enhancement of fresh fruit sample images at submicrometer pixel dimensions of 0.7 μm, enabling visualization of individual cell morphology, cell walls, and void networks. In addition to improving the resolution of void imaging significantly, the experiments were aimed to improve image contrast between voids and cells. Voids much smaller than 1-μm wide were, however, excluded from this study.

RESULTS

3-D Architecture of Pome Fruit Tissue

Figure 1 displays two-dimensional (2-D) tomographic slices of the cortex of apple and pear fruit at different spatial resolutions. In absorption imaging mode, the contrast between intercellular spaces and the cells was excellent (Fig. 1A). Phase contrast tomography at submicron pixel resolution results in images with sharp edges between voids and cells (Fig. 1B). Cell walls between adjacent cells are visible in the phase contrast images, allowing segmentation of tissues into individual cells. The apple cortex contains considerably larger parenchyma cells and voids than pear parenchyma. Voids in apple often appear larger than surrounding cells and some cells are not connected to an intercellular space. Voids in pear cortex tissue, in contrast, are always smaller than parenchyma cells, but each cell is surrounded by voids. Parenchyma cells in pear have a round shape without distinctive corners, thus leaving a space for voids that have, from small to large, triangular, rectangular, and few polygonal cross sections with concave sides, suggesting mainly schizogenous void formation (Raven, 1996). Apple parenchyma cells more often appear in distorted shapes and one is more likely to find touching cell corners in apple without an air void. The majority of the voids in apple cortex tissue have large polygonal concave cross sections, indicating a lysigenous origin (Raven, 1996).

Figure 2 presents the 3-D rendering of parenchyma cells and the surrounding voids of apple and pear fruit, respectively, as obtained by segmenting the phase contrast images (Supplemental Movies S1a

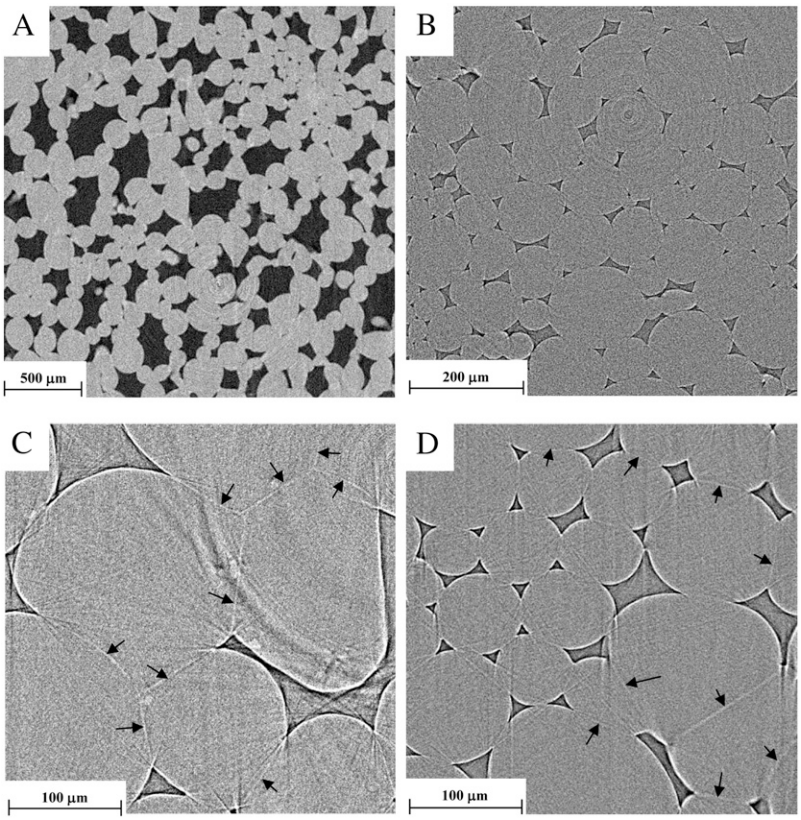

Figure 1. A to D, Tomographic images of the cortex of apple (A and C) and pear (B and D). Shown are slices (512 × 512 pixels) obtained by absorption tomography (A and B), at 5- and 1.4-μm pixel resolution for apple and pear, respectively, and phase contrast tomography (C and D) at 700-nm pixel size. Dark regions are gas-filled intercellular spaces; light regions are cells. Cell walls (indicated by arrows) between adjacent cells can be distinguished in the phase contrast images and are specifically clear in apple cortex.

and S1b). Apart from the size and shape difference, the difference in void-to-cell connection is especially apparent. Although the voids lie like wires of a tight net around the pear cell (Fig. 2B), a small number of larger voids connect in an irregular disconnected pattern to the apple cell (Fig. 2A).

Void Networks

Segmentation of the void network of pome fruit was achieved using a manually chosen constant threshold on absorption images. 3-D representations of the void networks in the cortex of different fruit are given in Figure 3 (see also Supplemental Movies S2a and S2b). We show for the first time that not only the shape and size of the voids differ between apple and pear. The connectivity of the network is substantially different in the two fruits. Voids between apple parenchyma form an incompletely connected network (Fig. 3A), confirming previous results (Mendoza et al., 2007) but now with much better contrast and resolution. Void spaces can be long and may stretch over several hundreds of micrometers in the tissue. These voids do not connect or split, but are surrounded by smaller

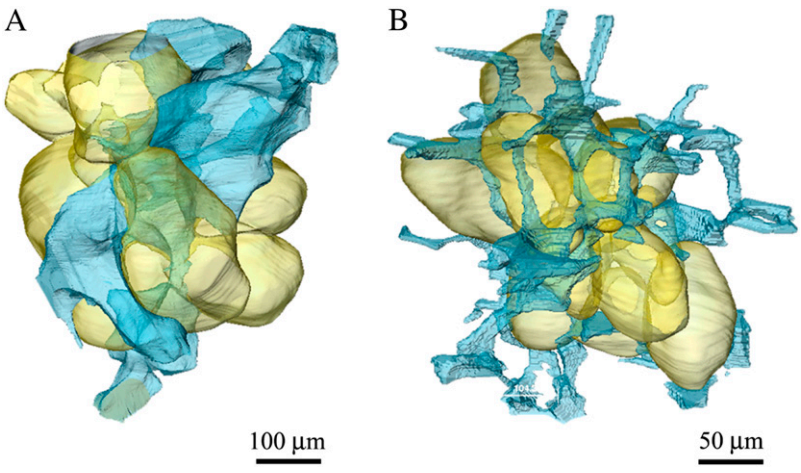

Figure 2. A and B, 3-D rendering of parenchyma tissue and single cells (in yellow) of apple (A) and pear (B) with adjacent voids (in blue). Images obtained from phase contrast tomography. While the voids lie like wires of a tight net around the pear cell, a small number of larger voids connect in an irregular disconnected pattern to the apple cell.

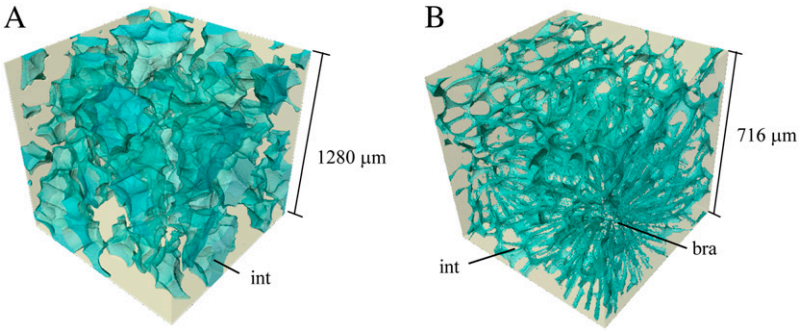

Figure 3. A and B, 3-D rendering of the void network of apple (A) and pear (B) fruit cortex. The marked components are the intercellular void spaces (int) and the brachysclereids (bra). While the voids between apple parenchyma are large and form an incompletely connected network, those of pear are very small and form a complete network throughout the cortex sample without preferential direction.

individual voids without preferential direction. On the equator of the apple fruit where the samples were taken, the axes of the long voids in the cortex tissue are preferentially oriented in the radial direction into the fruit.

In contrast, although the void fraction of pear is very small, the pores form a complete network throughout the cortex sample without preferential direction (Fig. 3B). Figure 3B essentially exists of structural units as shown in Figure 2B. The degree of connectivity exceeds that found in seeds (Cloetens et al., 2006) or other fruit (Kuroki et al., 2004). However, one particular feature disturbs the network pattern to a large extent. The characteristic brachysclereids (stone cells) that appear frequently in pear fruit cortex have a large effect on the void network architecture. Figure 3B displays in the bottom right corner the radially oriented stretched voids that surround a brachysclereid group. Sclereids are small cells that cease growth during fruit maturation, which is associated with a strong lignification of the cell wall. The surrounding cells that continue to grow evolve into elongated shapes, leading to the observed void network pattern. There are very little or no voids in between the brachysclereids themselves.

The other tissues show very similar differences between apple and pear. The void architecture of the subepidermis outer cortex layers is similar to the main cortex region in both fruits (Fig. 4). However, the cells of the outer cortex are smaller and packed in a denser pattern. This results in a less connected void network for pear, and a smaller volume fraction of the voids in

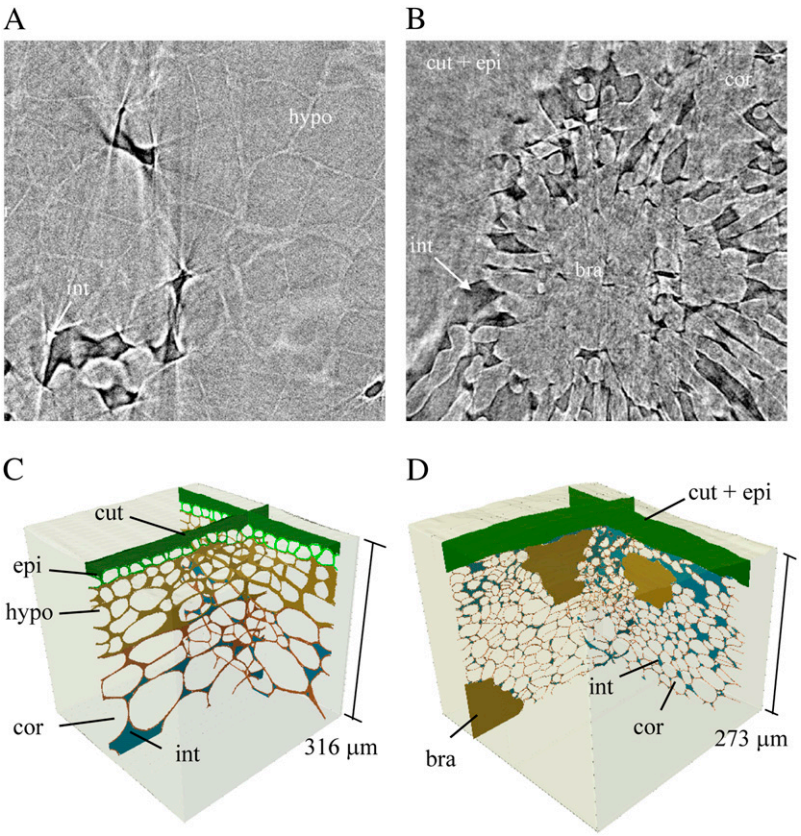

Figure 4. A and B, Epidermis and outer cortex of apple (A) and pear (B), obtained from phase contrast imaging at 700-nm voxel resolution. The components are marked as cuticle (cut), epidermis (epi), hypodermis (hypo), cortex (cor), intercellular spaces (int), and brachysclereids (bra). The top figures are raw tomographic 2-D slices (512 × 512 pixels) taken through the sample, showing the transition from cortex to hypodermis (apple) and to epidermis (pear). C and D, Structural 3-D models obtained from the images.

both fruits (Drazeta et al., 2004a; Schotsmans et al., 2004). Furthermore, brachysclereids (Fig. 4, B and D) are seen much more abundantly just beneath the epidermis of pear, resulting in many interrupted radial void networks of the type discussed in the previous paragraph. In apple fruit (Fig. 4, A and C) we found four layers of tightly packed collenchyma cells below the epidermis. The considerably thickened cell walls are clearly visible from the phase contrast images, mainly at the cell corners. This region is completely without voids. In pear, the void network extends to the epidermis, which itself could not be distinguished from the cuticle (Fig. 4, B and D). Cell wall thickening does not occur in the pear hypodermis.

The vascular bundles of the fruit run from the stem to the calyx through the cortex. The 3-D void and cellular architecture of vascular tissue in apple and pear fruit is displayed in Figure 5. In harvested pear fruit (Fig. 5, B and D), the xylem vessels are voids, and their characteristic lignified cell wall exhibits a spiral thickening pattern. Twenty to 30 vessels are grouped with dense elongated xylem parenchyma without voids (Lang and Ryan, 1994). The concentric phloem consists of cells stacked in a tight pattern without intercellular void spaces. The phloem cells are filled with liquid. The bundle is surrounded by cortex tissue consisting of increasingly larger cells away from the bundle, and with the typical void architecture. Vascular tissue of apple is similar (Fig. 5, A and C), but contains less but wider vessels that are sometimes discontinuous in the axial direction, which has been observed to occur during growth (Drazeta et al., 2004b). The surrounding phloem does not contain voids and the voids of the neighboring parenchyma are not connected. The individual void volumes in the parenchyma tissue are considerably smaller than the voids of the cortex (Fig. 3A).

Fruits of different maturity were analyzed. A total of three cortex samples from each of three different fruits for each development stage were measured. The resulting evolution in porosity is given in Figure 6. We did not find a significant difference in porosity between the fruits of the different development stages approaching and beyond picking maturity. Another remarkable result is that the ripening of the fruit in shelf life does not affect the porosity of the cortex. Although pears left on the shelf for 6 d soften significantly, the cells maintain their structure and water loss into the intercellular void space does not occur.

DISCUSSION

With this method we are able to visualize air voids that are as small as 1 μm. This should be sufficient to identify voids of lysigenous origin, producing air spaces where cells have died. Schizogenous aerenchyma results from cells separating, and the control mechanism for its development is not well understood (Jackson and Armstrong, 1999; Evans, 2003). However, as the middle lamellae separate during formation of these intercellular spaces, these pores have an infinitesimal small size limit at their time of birth. These smallest pores cannot be visualized with this method, but it is unlikely that they will be important for gas exchange. One, they are too small to add a significant contribution to the overall diffusion. Two, they would probably be isolated from the main pore network. For the mature fruits that were measured, the question, however, arises whether void spaces are still generated

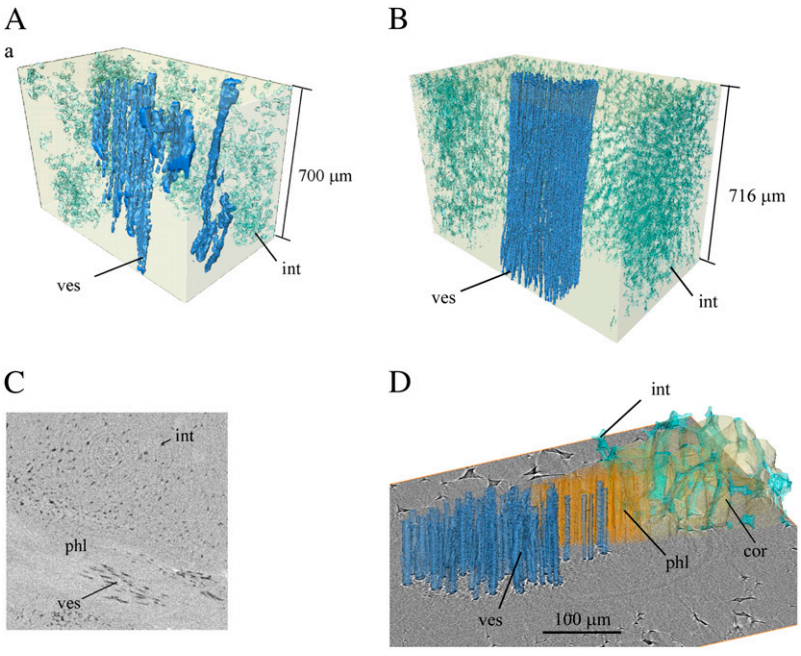

Figure 5. A to D, 3-D rendering of the vascular tissue of apple (A and C) and pear (B and D). The images are obtained from tomography in absorption mode at 1.4-μm voxel resolution (A and C) and at 5-μm voxel resolution (B). Image D is segmented from phase contrast images at 700-nm voxel size. The components are marked as cortex (cor), intercellular spaces (int), xylem vessels (ves), and phloem (phl). Image C is a raw 2-D horizontal tomographic slice (400 × 400 pixels) through the apple sample.

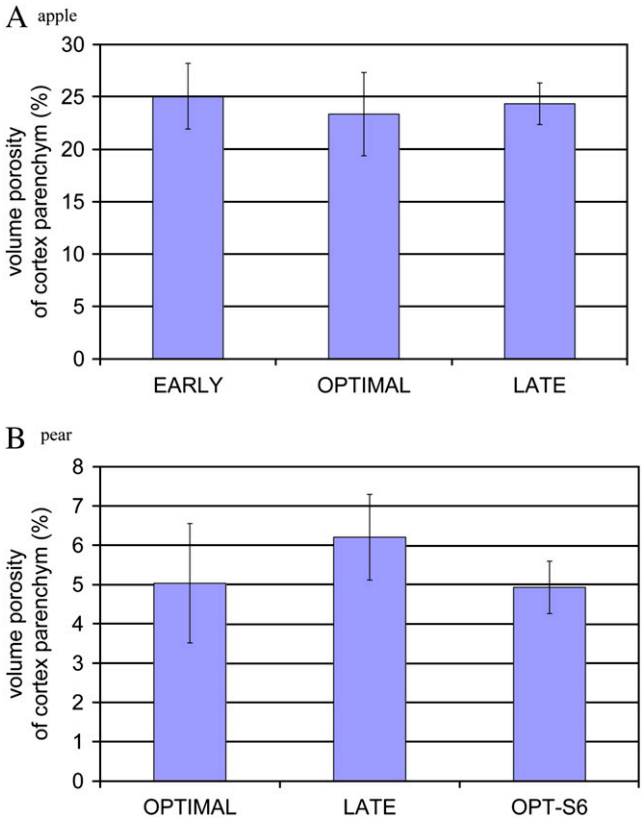

Figure 6. Volume porosity of the cortex parenchyma tissue of apple (A) and pear (B) as a function of maturity. Fruits were harvested from 14 d before (EARLY) to 14 d after (LATE) the commercial preclimacteric picking date (OPTIMAL). OPT-S6 corresponds to fruits that were measured after 6 d of shelf life at room temperature. The other fruits were preserved optimally in controlled atmosphere conditions at low temperature. [See online article for color version of this figure.]

and growing at this development stage. If not, it is unlikely that there are any such very small pores in the fruit. Considering the results in Figure 6, we can assume that at maturity void formation has completed because no effect of the maturity stage is seen on void fraction. Fruit at different growth stages should be analyzed next to investigate the organogenesis of aerenchyma in earlier stages of development.

This is, to our knowledge, the first work that quantifies 3-D voids in pome fruit at different development stages. Furthermore, these results also contribute to make progress in understanding and describing void formation in fruits. Current research questions in this field are dedicated to the processes initiating and regulating cell separation and cell death leading to specialized aerenchyma in plant tissues (Evans, 2003). The measurements support the hypothesis that aerenchyma formation in plant organs is mainly a result of a programmed process that is part of their development. The following reasons can be given. First, the void networks in pear and apple fruit are totally different, although both fruits are grown in similar climate and soil conditions. Second, the particular void structure is consistent over different samples and fruits.

The schizogeny in pear is similar throughout the cortex, indicating that all parenchyma cells have a control mechanism of ordered growth and division to create a continuous gas space. Synchrotron x-ray computed tomography can next be applied to visualize the cell growth and separation in early stages of pear fruit development to help unravel the development process.

This study provides no evidence whether the void network in apple stems from extreme schizogeny or lysigeny, and whether this is a constitutive mechanism or induced by other stimuli. First, from research on roots we know that it is difficult to observe any structural features that set cortex cells dedicated to die apart from their neighbors, which could be in support of lysigenous void formation (Inada et al., 2002). The mechanism of formation of lysigenous aerenchyma by induction from external and internal factors is currently receiving considerable support in the literature (Evans, 2003). In roots, hypoxia has been suggested as an important condition for void formation (Jackson et al., 1985). The cell death is not merely due to the oxygen starvation (Gunawardena et al., 2001): rather it is a result from the initiation of a cell death pathway that can be triggered also by other factors such as ethylene, or deficiency of nitrate and phosphate (Drew et al., 1989). Low oxygen stress may occur as the fruit grows and the resistance to diffusion of oxygen from the atmosphere through the skin and the thickening cell layers of the cortex becomes significant. O_2 gradients have been observed in plant organs such as roots, tubers, stems, inflorescences, seeds, and fruit (Sinclair and Goudriaan, 1981; Drew, 1997; Porterfield et al., 1999; Geigenberger et al., 2000; Seymour, 2001; Lammertyn et al., 2003; Van Dongen et al., 2003). In bulky storage organs such as fruit, where the length of the diffusion path may be considerable, hypoxic conditions have been demonstrated (Ho et al., 2008).

Aerenchyma formation under hypoxia is stimulated by a number of stresses. Among factors inducing cell death, ethylene has been attributed a major role (Gunawardena et al., 2001). It has been suggested that cells programmed to die are equipped with ap-

Table I. *Mean values and* SD *of apparent oxygen diffusivity in the cortex and the skin of apple Jonagold and pear Conference*

	D_{O_2}			
	Apple		Pear[a]	
	Cortex	Skin	Cortex	Skin
	($\times 10^{-9}$ m^2 s^{-1})			
Radial	7.1 ± 4.6 (n = 8)	0.19 ± 0.13 (n = 8)	0.28 ± 0.15 (n = 8)	0.10 ± 0.03 (n = 8)
Vertical	2.1 ± 1.0 (n = 7)	–	–	–
Vascular	4.2 ± 2.2 (n = 9)		1.1 ± 0.7 (n = 7)	

[a]Ho et al. (2006).

propriate receptors for ethylene (Evans, 2003). Ethylene is present in fruit where it initiates the ripening process of climacteric fruits, such as pear and apple, after growth (Génard and Gouble, 2005), and increases sharply at this stage. Because apple fruit at different stages of maturity did not show any difference in void space, it is not likely that ripening affects void formation. There is, however, little information on internal ethylene levels and gradients during fruit growth. Further, recent studies provided evidence that effects thought to be caused by ethylene are rather caused by nitric oxide (Igamberdiev and Hill, 2004; Borisjuk et al., 2007). Nitric oxide, in turn, is known to induce programmed cell death (Hoeberichts and Woltering, 2002; Neill et al., 2003). A combined tomography and internal gas analysis during fruit growth is hence needed to make progress on the understanding of void formation in fruit.

The mean calculated volume fraction of voids in the images of the cortex equals 5.1% ± 1.5% (SD) for pear and 23.0% ± 4.0% (SD) for apple, confirming previous studies (Ho et al., 2006; Mendoza et al., 2007). The ability of the cortex tissue to facilitate oxygen exchange, expressed by the apparent oxygen diffusivity, does not scale linearly with this value: the apparent radial oxygen diffusivity of pear (Ho et al., 2006) and apple cortex in the preclimacteric development stage and position in the two fruits equals $2.8 \pm 1.5 \times 10^{-10}$ (SD) $m^2 s^{-1}$ ($n = 6$) and 70.9 ± 45.6 (SD) $\times 10^{-10}$ $m^2 s^{-1}$ ($n = 8$), respectively. Measurements also indicate that oxygen diffusivity of apple cortex is higher in the radial direction than in the axial direction (Table I), which is confirmed by the preferential orientation of the void spaces found in the tomographic images. The structure of the other tissues also relate in a complex manner to gas exchange mechanisms. Skin tissue samples, comprising cuticle, epidermis, and outer cortex, have a smaller effective diffusivity than cortex tissue. However, the values for pear and apple are in the same range: $1.0 \pm 0.3 \times 10^{-10}$ (SD) $m^2 s^{-1}$ ($n = 8$) for pear (Ho et al., 2006) and $1.9 \pm 1.3 \times 10^{-10}$ (SD) $m^2 s^{-1}$ ($n = 8$) for apple (Table I). The differences in microstructure of pear and apple in the skin region, therefore, appear to be less important for the global gas exchange of the fruit. The skin barrier for gas exchange is large in both fruits due to the dense tissue structure (with a void volume fraction of <5% in both fruits) and the cuticle. Axial diffusivity of vascular tissue of pear was found previously to be considerably larger than that of cortex tissue: a value of 11.1 ± 7.1 (SD) $\times 10^{-10}$ $m^2 s^{-1}$ ($n = 7$) was measured (Ho et al., 2006). The presence of empty xylem vessels without considerable tortuosity does confirm this observation. In apple, the measurements reveal a nonsignificant difference between apparent diffusivity of vascular and cortex tissue (Table I). The discontinuity of the vessels and the dense phloem and cortex tissue in this region with a small amount of air voids (Fig. 5) are in line with this measured result.

In terms of facilitating gas exchange, the network pattern of the voids in pears (Fig. 3B) is by far not sufficient to compensate for the large size and volume fraction difference with the unconnected void structure we find in apple (Fig. 3A). Indeed, regardless of its ingenious architecture, even the partial breakdown of such networks will quickly lead to an internal gas imbalance. These results will at least partially explain the larger sensitivity of pears to physiological disorders related to gas exchange (Lammertyn et al., 2003; Ho et al., 2008). Surprisingly, physiological disorders that appear during storage, such as browning, initiate in or near the vascular tissue (Lammertyn et al., 2003), although this tissue has larger diffusivity for gases. We believe this is related to the high resistance for gas exchange and low oxygen concentration of the phloem and supporting cells of the xylem as a result of the complete lack of voids in these zones (Van Dongen et al., 2003), in addition to the small void fraction in the nearest layers of parenchyma cells (Fig. 5).

The images obtained here provide the necessary geometric information to use in a theoretical framework to confirm the results for gas exchange (Wood et al., 2000). To achieve this goal, advanced image analysis tools are today available to characterize the void structure in terms of pore size distribution and connectivity (Mendoza et al., 2007), and to transform the images into computer models by means of tessellation algorithms (Mebatsion et al., 2006).

Synchrotron x-ray tomography permitted noninvasive 3-D inspection of samples in their natural state. The field of view of the presented images was on the order of 1 mm; the samples were cylinders of 5-mm diameter. The measurement time for each sample was close to 15 min, after which reconstruction and segmentation of the images had to be performed by dedicated software and trained personnel. With this resolution and contrast, it is impossible to view intracellular features, or quantify the thickness and structure of cell walls. This is a drawback in comparison to electron tomography (ET) that, however, works on even much smaller samples. Therefore, the applicability of ET for investigating mesoscale structures such as void networks that extend throughout tissue is limited. ET will be appropriate for studying subcellular aspects. O'Toole et al. (1999) used ET to visualize organelles in cultured yeast cells at a resolution of 5 nm. The method requires cell preparation, slicing, staining, and coating. The method has only recently been introduced to plant sciences for investigating cell wall structure and cell organelles (Otegui et al., 2001; Seguí-Simarro et al., 2004; Xu et al., 2007).

MATERIALS AND METHODS

Tomography Experiments

Samples

Pears (*Pyrus communis* 'Conference') were harvested on September 13, 2006, at the experimental station Fruitteeltcentrum (Rillaar, Belgium). Apples *Malus* × *domestica* 'Jonagold') were picked at the preclimacteric stage on September 25, 2006, at the experimental station PCFruit (Velm, Belgium).

Fruits of "Early" and "Late" picking dates were harvested 14 d before and after the given dates, respectively. All fruits were cooled and stored under controlled atmosphere conditions (2.5 kPa O_2, 0.7 kPa CO_2 −1°C for pear; 1 kPa O_2, 2 kPa CO_2 0.8°C for apple) up to the time of the experiment on November 3 to 6, 2006. Picking data and cooling procedures are optimal commercial practices to preserve fruit quality during long-term storage. Cylindrical samples of 5-mm diameter and 1- to 2-cm length were removed from the different tissues of the fruits using a cork bore in the radial direction on the equator of the fruit. The samples were mounted in a polymethyl methacrylate tube and covered with polymer foil to avoid dehydration.

Synchrotron X-Ray Tomography

The experiments were conducted at beamline ID19 of the European Synchrotron Radiation Facility, i.e. a long (150-m) imaging beamline where the spatial coherence of the beam is particularly large (transverse coherence length on the order of 100 μm). This large coherence allows phase-contrast imaging where the phase of the x-ray beam transmitted by the sample is shifted due to the interaction with the electrons in the material. Imaging using phase contrast, as opposed to absorption contrast, is a powerful method for the investigation of light materials, but also to distinguish, in absorbing materials, phases with very similar x-ray attenuation but different electron densities (Cloetens et al., 1999, 2006). In this study, it is efficiently used for edge detection at cell-cell interfaces where absorption images have insufficient contrast.

The x-ray beam, generated from an 11-pole, variable gap, high-magnetic field wiggler, was monochromatized to 18 keV using an artificial multilayer monochromator. The selected detector device comprised a FReLoN camera; a 14-bit dynamic CCD camera with a 2,048 × 2,048 pixel chip. The camera was assisted by a shutter, an x-ray/visible light converter, and an optic system providing a field of view of 1.43 × 1.43 mm^2 and, without binning, an image pixel size of 0.7 μm. A total of 1,200 projections with an exposure time of 0.5 s was acquired for each sample during a continuous rotation over 180°. The incident x-ray flux was reduced below the threshold for unrecoverable specimen damage. A sample-detector distance of 35 mm was chosen to operate in phase contrast mode. The tomographic reconstruction was performed with a filtered back-projection algorithm using the PyHST (ESRF) software, after correction for sample motion using GNU Octave software (http://www.gnu.org/software/octave/). Volume renderings and quantitative measurements on the sample were obtained by 3-D image segmentation and isosurface representations with Amira (Mercury Computer Systems).

Apparent Oxygen Diffusivity of Apple Cortex Tissue

Samples

Jonagold apples were harvested at the preclimacteric stage on September 9, 2006 at the experimental garden of PCFruit in Velm, Belgium. Apples were cooled and stored in optimal controlled atmosphere conditions (1% O_2, 2.5% CO_2) at 1°C, until they were used for experiments. Picking data and cooling procedures are optimal commercial practices to preserve fruit quality during long-term storage.

Samples of cortex tissue were first cut with a professional slice cutter (EH 158-L; Graef), from which cylinders with a diameter of 2.5 cm were cut with a cork borer. The thickness of samples ranged from 2 to 3 mm, measured with a digital caliper (accuracy ±0.01 mm; Mitutoyo). Cortex tissue samples were taken in the radial and vertical direction at the equatorial region of the apple. Skin samples were taken as outlined above, but included only cuticle to outer cortex cell layers. Cylindrical samples with a thickness on the order of 1 mm were obtained by means of a razor blade. Vascular samples were taken near the apex and the stem of the fruit, and outside the core.

Diffusivity Measurement

Apparent diffusivity along the axial direction of the samples was measured with the setup and procedures developed by Ho et al. (2006). The measured value comprises the combined effects of basic gas diffusivities in air and water and tissue microstructure. The system used to measure gas transport properties of fruit tissue consisted of two chambers (measurement chamber and flushing chamber) separated by the disc-shaped tissue sample. The chambers were metal cylinders screwed together, holding a polyvinyl chloride ring glued to the sample with cyano-acrylate glue. A rubber O-ring was used to seal the polyvinyl chloride ring between the two chambers and to ensure that all gas transport between the two chambers took place through the tissue sample. Two inlet and outlet gas channels were used to flush the gases in the measurement chamber and flushing chamber. Pressure sensors (PMP 4070, accuracy ±0.04%; GE Druck) monitored the pressure changes in each chamber during the measurements. The temperature of the system was kept constant at 20.0 ± 0.5°C by submerging the setup in a temperature-controlled water bath (F10-HC, accuracy ±0.5°C; Julabo Labor Technik GmbH). Sealing of chambers was checked and validated before the experiments.

Once the sample was attached to the diffusion cell, the measurement and the flushing chambers were flushed with, respectively, 69 kPa N_2, 30 kPa O_2, 1 kPa CO_2 and 85 kPa N_2, 10 kPa O_2, 5 kPa CO_2, at 10 L h^{-1} humidified and passed through a heat exchanger to prevent the sample from drying and cooling down while flushing the two chambers. After 30 min, the inlet and outlet valves of the measurement chamber were closed, and the decrease in O_2 partial pressure, the increase in CO_2 partial pressure, and total pressure of the measurement chamber was monitored for 6 h with steps of 20 s. The O_2 and CO_2 concentrations were measured in the measurement chamber with fluorescent optical probes (Foxy-Resp and FCO2-R; Ocean Optics). The difference in total pressure between the two chambers was logged (PMP 4070; GE Druck) and was kept smaller than 1.5 kPa to minimize permeation.

D_{o_2} and D_{co_2} were estimated by fitting the solution of the following transport equation for O_2 and CO_2 to the measured concentration profiles in the measurement chamber:

$$\frac{\partial C}{\partial t} = D\nabla^2 C + R \tag{1}$$

$$D\frac{\partial C}{\partial n} = h(C_\infty - C) \text{ at } \Gamma \tag{2}$$

where $\partial/\partial n$ denotes partial derivative in the outward normal direction; C is the oxygen or carbon dioxide concentration (mol m^{-3}); D is the diffusion coefficient (m^2 s^{-1}); R is the oxygen consumption or carbon dioxide production (mol m^{-3} s^{-1}); ∇^2 is the Laplace operator (m^{-2}); h is the convective mass transfer coefficient (m s^{-1}); t is the time (s); and Γ is the surface of the tissue exposed to the flushing chamber. Index ∞ refers the gas atmosphere in the flushing chamber.

Equations 1 and 2 were solved using the finite element method in one dimension using the Comsol finite element code (COMSOL Multiphysics). The gas in the measurement chamber and the sample tissue were considered as two materials consisting of 20 elements each resulting in 41 nodes in total. The diffusion coefficient of the gas molecules in air at 20°C was equal to 6 × 10^{-5} m^2 s^{-1}. The sample was modeled as the second material, for which the diffusion coefficient was to be estimated. The gas transfer from the flushing chamber to the tissue or the skin was expressed by Equation 2 as a convection boundary condition. The convective mass transfer coefficient was taken very high (1 × 10^6 m/s). This means it was assumed that no resistance to gas transport occurred at this interface.

An iterative least squares estimation procedure written in MATLAB (The Mathworks) was used to determine gas diffusivities of the pear tissues by fitting the model solutions to the measured O_2 and CO_2 concentration change profiles.

Respiration Kinetics

A noncompetitive inhibition model (Ho et al., 2006) was used to describe the respiration rates R of the tissue. Samples of fruit cortex tissue were first cut with a professional slice cutter (EH 158-L; Graef), from which cylinders with a diameter of 2.5 cm were cut with a cork borer. Cylindrical samples were taken with a thickness of 2 to 3 cm, which was measured with a digital caliper (accuracy ±0.01 mm; Mitutoyo). Apple tissue samples were placed in airtight glass jars. Three jars of the same gas mixture and temperature according to the experimental design were connected in series. Then, the jar headspace was flushed continuously with a gas mixture at a flow rate of 20 L/h for an adaptation period of 1 1/2 h. After that, the jars were closed and the initial headspace was measured for O_2 and CO_2 partial pressure (kPa) with a gas analyzer (CheckMate II; PBI Dansensor) and for total pressure (PTX1400; Druck). The headspace was measured again after 12, 30, and 48 h of incubation for samples incubated at a temperature of 20°C, 10°C, and 5°C, respectively. Because the respiration rate was calculated as mol s^{-1} m^{-3}, the difference in partial pressure was converted to molar concentration using the ideal gas law; the free gas volume in the respiration jar was calculated by subtracting the

total jar volume from the total sample volume. The sample volume was calculated by multiplying the tissue weight with the density of the apple fruit. The density of the fruit was measured by the water displacement method. The measured respiration rate at different gas concentrations was used to estimate the parameters of the respiration kinetics described in Ho et al. (2006). Respiration model parameters were estimated by fitting the model equations to the experimental data using the nonlinear least square estimation procedure of Matlab (Matlab 7.0; The Mathworks).

Supplemental Data

The following materials are available in the online version of this article.

Supplemental Movie S1. 3-D rendering of single cells (in magenta) of apple (a) and pear (b) with adjacent voids (in yellow).

Supplemental Movie S2. 3-D rendering of the void network of apple (a) and pear (b) cortex.

ACKNOWLEDGMENT

We thank Thang Manh Khuong for assistance during gas exchange measurements.

Received March 10, 2008; accepted April 13, 2008; published April 16, 2008.

LITERATURE CITED

Aalto T, Juurola E (2002) A three-dimensional model of CO_2 transport in airspaces and mesophyll cells of a silver birch leaf. Plant Cell Environ **25:** 1399–1409

Abbott A (2003) Cell culture: biology's new dimension. Nature **424:** 870–872

Attwood D (2006) Microscopy—nanotomography comes of age. Nature **442:** 642–643

Borisjuk L, Macherel D, Benamar A, Wobus U, Rolletschek H (2007) Low oxygen sensing and balancing in plant seeds—a role for nitric oxide. New Phytol **176:** 813–823

Cloetens P, Ludwig W, Baruchel J, Van Dyck D, Van Landuyt J, Guigay JP, Schlenker M (1999) Holotomography: quantitative phase tomography with micrometer resolution using hard synchrotron radiation x rays. Appl Phys Lett **75:** 2912–2914

Cloetens P, Mache R, Schlenker M, Lerbs-Mache S (2006) Quantitative phase tomography of Arabidopsis seeds reveals intercellular void network. Proc Natl Acad Sci USA **103:** 14626–14630

Colmer TD (2003) Long-distance transport of gases in plants: a perspective on internal aeration and radial oxygen loss from roots. Plant Cell Environ **26:** 17–36

Davis TJ, Gao D, Gureyev TE, Stevenson AW, Wilkins SW (1995) Phase contrast imaging of weakly absorbing materials using hard X-rays. Nature **373:** 595–598

Denison RF (1992) Mathematical modeling of oxygen diffusion and respiration in legume root nodules. Plant Physiol **98:** 901–907

Drazeta L, Lang A, Hall AJ, Volz RK, Jameson PE (2004b) Causes and effects of changes in xylem functionality in apple fruit. Ann Bot (Lond) **93:** 275–282

Drazeta L, Lang A, Hall AJ, Volz RK, Jameson PE (2004a) Air volume measurement of 'Braeburn' apple fruit. J Exp Bot **55:** 1061–1069

Drew MC (1997) Oxygen deficiency and root metabolism: injury and acclimation under hypoxia and anoxia. Annu Rev Plant Physiol Plant Mol Biol **48:** 223–250

Drew MC, He CJ, Morgan PW (1989) Decreased ethylene biosynthesis, and induction of aerenchyma, by nitrogen-starvation or phosphate-starvation in adventitious roots of *Zea mays* L. Plant Physiol **91:** 266–271

Evans DE (2003) Aerenchyma formation. New Phytol **161:** 35–49

Franck C, Lammertyn J, Ho QT, Verboven P, Verlinden B, Nicolaï BA (2007) Browning disorders in pear: a review. Postharvest Biol Technol **43:** 1–13

Fukao T, Bailey-Serres J (2004) Plant responses to hypoxia—is survival a balancing act? Trends Plant Sci **9:** 449–456

Geigenberger P, Fernie AR, Gibon Y, Christ M, Stitt M (2000) Metabolic activity decreases as an adaptive response to low internal oxygen in growing potato tubers. Biol Chem **381:** 723–740

Génard M, Gouble B (2005) ETHY. A theory of fruit climacteric ethylene emission. Plant Physiol **139:** 531–545

Gunawardena A, Pearce DM, Jackson MB, Hawes CR, Evans DE (2001) Characterisation of programmed cell death during aerenchyma formation induced by ethylene or hypoxia in roots of maize (Zea mays L.). Planta **212:** 205–214

Ho QT, Verboven P, Verlinden BE, Lammertyn J, Vandewalle S, Nicolaï BM (2008) A continuum model for gas exchange in pear fruit. PLoS Comput Biol **4:** e1000023

Ho QT, Verlinden BE, Verboven P, Vandewalle S, Nicolaï BM (2006) A permeation-diffusion-reaction model of gas transport in cellular tissue of plant materials. J Exp Bot **57:** 4215–4224

Hoeberichts FA, Woltering EJ (2002) Multiple mediators of plant programmed cell death: interplay of conserved cell death mechanisms and plant-specific regulators. Bioessays **25:** 47–57

Igamberdiev AU, Hill RD (2004) Nitrate, NO and haemoglobin in plant adaptation to hypoxia: an alternative to classic fermentation pathways. J Exp Bot **55:** 2473–2482

Inada N, Sakai A, Kuroiwa H, Kuroiwa T (2002) Three-dimensional progression of programmed death in the rice coleoptil. Int Rev Cytol **218:** 221–258

Jackson MB, Armstrong W (1999) Formation of aerenchyma and the processes of plant ventilation in relation to soil flooding and submergence. Plant Biol **1:** 274–287

Jackson MB, Fenning TM, Drew MC, Saker LR (1985) Stimulation of ethylene production and gas-space (aerenchyma) formation in adventitious roots of Zea mays L. by small partial pressures of oxygen. Planta **165:** 486–492

Kim SA, Punshon A, Lanzirotti A, Li L, Alonso JM, Ecker JR, Kaplan J, Guerinot ML (2006) Localization of iron in Arabidopsis seed requires the vacuolar membrane transporter VIT1. Science **314:** 1295–1298

Kuroki S, Oshita S, Sotome I, Kawagoe Y, Seo Y (2004) Visualization of 3-D network of gas-filled intercellular spaces in cucumber fruit after harvest. Postharvest Biol Technol **33:** 255–262

Lammertyn J, Scheerlinck N, Jancsók P, Verlinden BE, Nicolaï BM (2003) A respiration-diffusion model for 'Conference' pears II: Simulation and relation to core breakdown. Postharvest Biol Technol **30:** 43–55

Lang A, Ryan KG (1994) Vascular development and sap flow in apple pedicels. Ann Bot (Lond) **74:** 381–388

Larabell GA, Le Gros MA (2003) X-ray tomography generates 3-D reconstructions of the yeast, *Saccharomyces cerevisiae*, at 60-nm resolution. Mol Biol Cell **15:** 957–962

Lawson T, Morison J (2006) Visualising patterns of CO_2 diffusion in leaves. New Phytol **169:** 641–643

Mebatsion HK, Verboven P, Ho QT, Mendoza F, Verlinden BE, Nguyen TA, Nicolaï BM (2006) Modeling fruit microstructure using novel ellipse tessellation algorithm. CMES-Comp Model Eng **14:** 1–14

Mendoza F, Verboven P, Mebatsion HK, Kerckhofs G, Wevers M, Nicolaï B (2007) Three-dimensional pore space quantification of apple tissue using X-ray computed microtomography. Planta **226:** 559–570

Miao JW, Hodgson KO, Ishikawa T, Larabell CA, LeGros MA, Nishino Y (2003) Imaging whole Escherichia coli bacteria by using single-particle x-ray diffraction. Proc Natl Acad Sci USA **100:** 110–112

Neill SJ, Desikan R, Hancock JT (2003) Nitric oxide signaling in plants. New Phytol **159:** 11–35

Otegui MS, Mastronarde D, Kang BH, Bednarek SY, Staehelin LA (2001) Three-dimensional analysis of syncytial type cell plates during endosperm cellularization visualized by high resolution electron microscopy. Plant Cell **13:** 2033–2051

O'Toole ET, Winey M, McIntosh JR (1999) High-voltage electron tomography of spindle pole bodies and early mitotic spindles in the yeast Saccharomyces cerevisiae. Mol Biol Cell **10:** 2017–2031

Parkhurst DF, Mott KA (1990) Intercellular diffusion limits to CO_2 uptake in leaves: studies in air and helox. Plant Physiol **94:** 1024–1032

Plouraboue F, Cloetens P, Fonta C, Steyer A, Lauwers A, Marc-Vergnes JP (2004) X-ray high-resolution vascular network imaging. J Microsc **215:** 139–148

Porterfield DM, Kuang A, Smith PJS, Crispi ML, Musgrave ME (1999) Oxygen-depleted zones inside reproductive structures of Brassicaceae: implications for oxygen control of seed development. Can J Bot **77:** 1439–1446

Rau C, Robinson IK, Richter CP (2006) Visualizing soft tissue in the

mammalian cochlea with coherent hard X-rays. Microsc Res Tech **69:** 660–665

Raven JA (1996) Into the voids: the distribution, function, development and maintenance of gas spaces in plants. Ann Bot (Lond) **78:** 137–142

Salvo L, Cloetens P, Maire E, Zabler S, Blandin JJ, Buffiere JY, Ludwig W, Boller E, Bellet D, Josserond C (2003) X-ray micro-tomography an attractive characterisation technique in materials science. Nucl Instrum Methods Phys Res B **200:** 273–286

Saquet AA, Streif J, Bangerth F (2000) Changes in ATP, ADP and pyridine nucleotide levels related to the incidence of physiological disorders in 'Conference' pears and 'Jonagold' apples during controlled atmosphere storage. J Hortic Sci Biotechnol **75:** 243–249

Schotsmans W, Verlinden BE, Lammertyn J, Nicolaï BM (2004) The relationship between gas transport properties and the histology of apple. J Sci Food Agric **84:** 1131–1140

Seguí-Simarro JM, Austin JR, White EA, Staehelin LA (2004) Electron tomographic analysis of somatic cell plate formation in meristematic cells of *Arabidopsis* preserved by high-pressure freezing. Plant Cell **16:** 836–856

Seymour RS (2001) Diffusion pathway for oxygen into highly thermogenic florets of the arum lily *Philodendron selloum*. J Exp Bot **52:** 1465–1472

Shapiro D, Thibault P, Beetz T, Elser V, Howells M, Jacobsen C, Kirz J, Lima E, Miao H, Neiman AM, et al (2005) Biological imaging by soft x-ray diffraction microscopy. Proc Natl Acad Sci USA **102:** 15343–15346

Sinclair TR, Goudriaan J (1981) Physical and morphological constraints on transport in nodules. Plant Physiol **67:** 143–145

Stuppy WH, Maisano JA, Colbert MW, Rudall PJ, Rowe TB (2003) Three-dimensional analysis of plant structure using high-resolution X-ray computed tomography. Trends Plant Sci **8:** 2–6

Thurner P, Muller R, Raeber G, Sennhauser U, Hubbell J (2005) 3D morphology of cell cultures: a quantitative approach using micrometer synchrotron light tomography. Microsc Res Tech **66:** 289–298

Van Dongen JT, Schurr U, Pfister M, Geigenberger P (2003) Phloem metabolism and function have to cope with low internal oxygen. Plant Physiol **131:** 1529–1543

Westneat MW, Betz O, Blob RW, Fezzaa K, Cooper WJ, Lee WK (2003) Tracheal respiration in insects visualized with synchrotron x-ray imaging. Science **299:** 558–560

Wood BD, Quintard M, Whitaker S (2000) Calculation of effective diffusivities for biofilms and tissues. Biotechnol Bioeng **77:** 495–516

Xu P, Donaldson LA, Gergely ZA, Staehelin LA (2007) Dual-axis electron tomography: a new approach for investigating the spatial organization of wood cellulose microfibrils. Wood Sci Technol **41:** 101–116